

# Many-Body Quantum Zeno Effect and Measurement-Induced Subradiance Transition

Alberto Biella<sup>1,\*</sup> and Marco Schiró<sup>1,†</sup>

<sup>1</sup>JEIP, USR 3573 CNRS, Collège de France, PSL Research University,  
11 Place Marcelin Berthelot, 75321 Paris Cedex 05, France

(Dated: February 24, 2022)

It is well known that by repeatedly measuring a quantum system it is possible to completely freeze its dynamics into a well defined state, a signature of the Quantum Zeno Effect. Here we show that for a many-body system evolving under competing unitary evolution and variable-strength measurements the onset of the Zeno effect takes the form of a sharp phase transition. Using the Quantum Ising chain with continuous monitoring of the transverse magnetization as paradigmatic example we show that for weak measurements the entanglement produced by the unitary dynamics remains protected, and actually enhanced by the monitoring, while only above a certain threshold the system is sharply brought into an uncorrelated Zeno state. We show that this transition is invisible to the average dynamics, but encoded in the rare fluctuations of the stochastic measurement process, which we show to be perfectly captured by a non-Hermitian Hamiltonian which takes the form of a Quantum Ising model in an imaginary valued transverse field. We provide analytical results based on the fermionization of the non-Hermitian Hamiltonian in supports of our exact numerical calculations.

**Introduction** – Measurements lie at the heart of quantum mechanics and of its intrinsic statistical interpretation [1]. They are known to fundamentally perturb the state of a quantum system, leading to the famous wave-function collapse, or to hamper its evolution in the Hilbert space, as in the celebrated Quantum Zeno Effect (QZE), where frequent projective measurements on a system can lead to its full localization [2–8]. In the field of quantum information the role of measurements as a resource has been extensively discussed and also experimentally demonstrated [9–13]. In the context of quantum many-body systems the interest is much more recent. Manifestations of many-body QZE have recently attracted interest [14–16]. A series of theoretical works have explored the interplay between entangling quantum many-body dynamics and frequent projective measurements, giving rise to novel exotic entanglement phase transitions [17–22]. A different measurement protocol is provided by a continuous monitoring, or variable strength weak measurements, which is defined in terms of positive operator-valued measurements (POVM) and provides a stochastic backaction onto the system [23, 24]. Also in this case entanglement phase transitions have been identified [19, 25]. A crucial feature of these transitions is that they are invisible to the average dynamics but only appears at the level of single quantum many-body trajectories.

In this Letter we address the competition between unitary many-body dynamics and stochastic quantum measurements in a simple and paradigmatic setting, namely when the two processes involve degrees of freedom which do not mutually commute, such as different components of a quantum spin. Surprisingly we find, in the context of a one-dimensional quantum Ising model with continuous monitoring of the local transverse magnetization, that the onset of the many-body QZE, in which the system

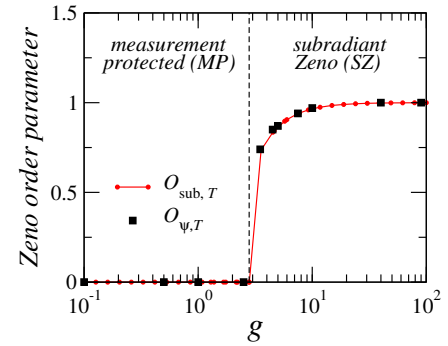


Figure 1. Order parameter for the onset of the many-body QZE. We plot the overlap between the long-time state and the Zeno state  $|T\rangle = \bigotimes_{i=1}^L |-\rangle_i$  as a function of the ratio between measurement and unitary evolution  $g = p_{\text{meas}}/J^x dt$ , for the full dynamics (squares) and for the non-Hermitian evolution (circles). Here we set  $p_{\text{site}} = 1, dt = 10^{-2}, L = 8, J^x = 1, N_{\text{real}} = 100$ .

is frozen by measurements into a well defined many-body state, appears sharply above a critical measurement strength (see Fig.1), a behavior suggestive of a novel form of quantum criticality. As for the above mentioned entanglement phase transitions, we show here that this sharp transition is encoded in the rare realizations of the stochastic process and cannot be observed by only looking at the average behavior of the system. We highlight this point by considering the no-click evolution, when the result of the measurements is not read and the dynamics can be described by a non-Hermitian Hamiltonian [26], which in our case takes the form of a non-Hermitian Transverse Field Ising Model (TFIM). Remarkably we show that the sharp onset of the many body QZE shown in Figure 1 can be understood in terms of a subradiance transition [27–33] in the many-body spectrum of the non-Hermitian TFIM, i.e. a non-analytic change in

the eigenstate with the smallest imaginary part. This result suggests an intriguing analogy with the concept of a quantum phase transition, where the system ground-state properties change abruptly as a result of the competition between non-commuting operators. We provide analytical arguments based on the fermionization of the non-Hermitian TFIM in supports of our exact numerical calculations.

**The Model and the measurement protocol** – In this work we consider a stochastic quantum many-body dynamics governed by the following protocol

$$|\psi(t + dt)\rangle = \hat{M}\hat{U}|\psi(t)\rangle, \quad (1)$$

where the unitary dynamics  $\hat{U} = \exp(-i\hat{\mathcal{H}}dt)$  is generated by a Quantum Ising model,

$$\hat{\mathcal{H}} = J^x \sum_{i=1}^{L-1} \hat{\sigma}_i^x \hat{\sigma}_{i+1}^x \quad (2)$$

( $\hat{\sigma}_i^\alpha, \alpha = x, y, z$  being the Pauli matrices acting on the  $i$ -th site) and  $\hat{M}$  is a measurement carried out simultaneously on each site with probability  $p_{\text{site}}$ . The operator  $\hat{M}$  is a (normalized) Kraus operator associated with a POVM. Specifically we have  $\hat{M} = \bigotimes_{i=1}^L \hat{M}_i^{(r)}$ , with  $r = 0, 1$  defined by

$$\begin{aligned} \hat{M}_i^{(0)} &= \hat{\Pi}_{i-}^z + \sqrt{1 - p_{\text{meas}}} \hat{\Pi}_{i+}^z, \\ \hat{M}_i^{(1)} &= \sqrt{p_{\text{meas}}} \hat{\Pi}_{i+}^z, \end{aligned} \quad (3)$$

where  $\hat{\Pi}_{i\pm}^z = (\mathbb{I} \pm \hat{\sigma}_i^z)/2$  are local projectors onto eigenstates of the spin  $z$ -component  $\hat{\sigma}_i^z |\pm\rangle_i = \pm |\pm\rangle_i$ . Locally, the probabilities of the two possible readouts are given by  $p_i^{(1)} = p_{\text{meas}} p_{\text{site}} \langle \Psi(t) | \hat{\Pi}_{i+}^z | \Psi(t) \rangle$ ,  $p_i^{(0)} = 1 - p_i^{(1)}$ .

Equations (1-3), together with the initial condition that we fix to be an uncorrelated state with all the spin aligned along the  $z$ -axis i.e.  $|\Psi(0)\rangle = \bigotimes_{i=1}^L |-\rangle_i$ , fully specifies the stochastic protocol we will focus on in this work. Each random realization provides a quantum many-body trajectory encoded in the wave function  $|\Psi(t)\rangle$ . We stress that Eq.(1) leads to an unnormalized wavefunction since  $\hat{M}$  is not a unitary operator. We thus normalize the quantum state after each step of the protocol.

In the following we are going to discuss the stochastic dynamics of the system as a function of the ratio between the frequency of the measurement and the unitary dynamics. It is natural therefore to introduce the adimensional control parameter

$$g = \frac{p_{\text{meas}}}{J^x dt}, \quad (4)$$

which will play a key role in the following. The physics in two limiting cases is easy to grasp. For  $g \ll 1$ , quantum jumps (the occurrence of  $\hat{M}_i^{(1)}$ ) take place with a very low

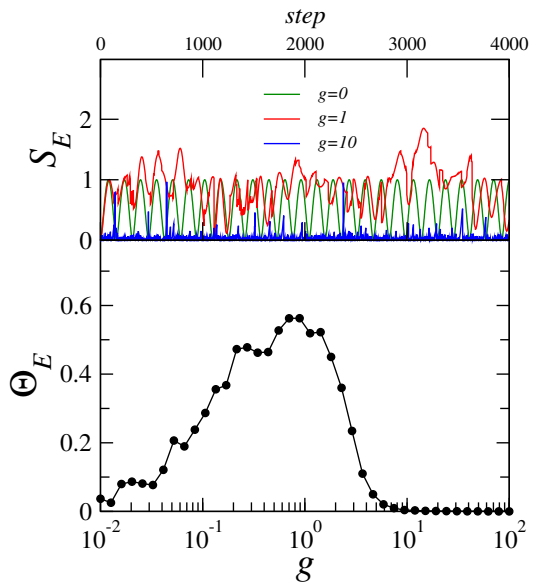


Figure 2. Top panel: Evolution of a single-trajectory entanglement entropy  $S_E(t)$  for different values of  $g$ . Bottom panel: measurement-induced entanglement  $\Theta_E$  as a function of  $g$ . Here we set  $N_{\text{real}} = 100, dt = 10^{-2}, L = 8, J^x = 1$ .

probability ( $p_{r=1} \ll 1$ ) regardless of the value of  $p_{\text{site}}$  and the projective measurement  $\hat{M}_i^{(0)}$  is close to the identity. The system therefore evolves under the unitary dynamics with rare measurements. In the opposite limit  $g \gg 1$  the measurements occur often with respect to the typical timescale settled by the unitary dynamics. In this regime the stochastic evolution starting from our initial condition stabilizes the uncorrelated state  $|T\rangle = \bigotimes_{i=1}^L |-\rangle_i$  which is also the exact fixed point of the measurement protocol in the limiting case  $p_{\text{meas}} = 1$ . As we are going to show below those two regimes are not smoothly connected, but a sharp phase transition between two well defined phases occur upon increasing  $g$ . Importantly, this will appear in the rare fluctuations but not in the average dynamics that instead display a rather featureless and smooth crossover.

**Results – Measurement-Induced Entanglement.** We start by studying the entanglement properties encoded in a single quantum many-body trajectory, as a function of  $g$ . Specifically, we compute the entanglement entropy of a symmetric bipartition of the system

$$S_E(t) = -\text{Tr}[\hat{\rho}_A(t) \log_2 \hat{\rho}_A(t)], \quad (5)$$

where  $\hat{\rho}_A(t) = \text{Tr}_B[|\psi(t)\rangle\langle\psi(t)|]$  is the reduced density matrix of the left halve (labelled as  $A$ ) of the system. In the purely unitary (and deterministic) case,  $g = 0$ , this quantity displays coherent Rabi oscillations in the range  $0 \leq S_E \leq 1$  (see Fig. 2, top panel). Remarkably, we find that for small finite  $g$  measurements can produce *more entanglement* between the two halves of the chain with respect to the unitary case, as shown by the single trajec-

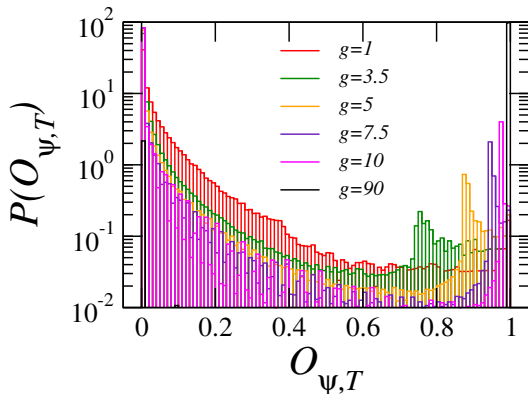


Figure 3. Probability distribution of the overlap  $O_{\psi,T} = |\langle \psi | T \rangle|$  between the long-time state and the Zeno state  $|T\rangle$ . Increasing the strength of the measurements  $g$  the distribution develops a secondary peak, which becomes dominant for large  $g$ . Here we set  $N_{\text{real}} = 100$ ,  $dt = 10^{-2}$ ,  $L = 8$ ,  $J^x = 1$ .

tory entanglement entropy going above  $S_E = 1$ . For large  $g$  instead, as expected, the entanglement production is strongly suppressed. In order to quantify this *entanglement generation* with respect to the unitary case ( $g = 0$ ) we consider the probability  $P(S_E)$  that a certain value of  $S_E$  occurs during the stochastic evolution and then we evaluate the measurement-induced entanglement  $\Theta_E$

$$\Theta_E = \int_{S_E > 1} S_E P(S_E) dS_E, \quad (6)$$

which is a measure of the entanglement generated on top of the unitary dynamics averaged over  $N_{\text{real}}$  stochastic realizations. In Fig.2 (bottom panel) we show the behavior of  $\Theta_E$  as a function of  $g$  and for  $p_{\text{site}} = 1$ . We find a surprising non-monotonic behavior of the excess entanglement as the strength of the measurements is increased, with a maximum around  $g \sim 1$  and a rapid decrease for larger value of  $g$ , ultimately expected as the QZE kicks in and the system is more and more projected towards the product state  $|T\rangle$ . A similar behavior is found for  $p_{\text{site}} \neq 1$ , as we discuss in Ref. [34] where we show in fact a data collapse suggesting the excess entanglement  $\Theta_E$  only depends on the product  $g p_{\text{site}}$ . This result shows that before the onset of the many body QZE the system at the single trajectory level is highly entangled, due to the interplay between unitary dynamics and measurements. As we are going to discuss below this result is the consequence of a transition between two phases, very different in nature, controlled by  $g$ .

*Onset of Many-Body Quantum Zeno effect* - As already discussed, for  $g \gg 1$  the measurements drive the system towards the uncorrelated product state  $|T\rangle$ , a signature of the QZE. We now discuss how the onset of Zeno emerge as the strength of the measurements is increased. To this extent we compute the probability distribution of the overlap  $O_{\psi,T} = |\langle \psi | T \rangle|$  at long times, that we plot

in Fig. 3 for different values of  $g$ .

For  $g \lesssim 1$  the function  $P(O_{\psi,T})$  is peaked at  $O_{\psi,T} = 0$ , signaling the correlated nature of  $|\psi(t)\rangle$  in the regime where the unitary quantum dynamics dominates, but display a skewed distribution with fat tails slowly decaying for larger value of  $O_{\psi,T}$ . The broad statistics of  $O_{\psi,T}$  suggests that taking the average overlap as measure of the onset of the QZE misses important aspects of the physics, and that atypical values of the overlap might play an important role in the stochastic dynamics. Remarkably for  $g \gtrsim 1$  a second peak emerges at  $O_{\psi,T} > 0$  and the distribution acquires a strong bimodal character. As  $g$  is increased further into the deep Quantum Zeno regime this secondary peak evolves and eventually becomes the dominant one. In Fig.1 we plot the position of this finite overlap peak as a function of  $g$  and find a remarkably sharp transition around  $g \sim 4$ , signaling the onset of the Zeno effect. We stress that the onset of the Zeno effect can be also studied in the stochastic dynamics of local observables, such as the local magnetization  $m_z$ . The probability distribution features a rich dynamics where the Zeno effect appears in stages [8], as we discuss more in Ref. [34].

*No-click dynamics and subradiance transition.* We now provide further insights into this transition by considering the no-click case, i.e. when the result of the measurements is not read. In this case  $\hat{M} = \bigotimes_{i=1}^L \hat{M}_i^{(0)}$  regardless of the value of the system parameters. For  $dt \rightarrow 0$  the no-click evolution can be described by an effective non-hermitian Hamiltonian  $\hat{\mathcal{H}}_{\text{eff}}$  that can be obtained from equation (1). We checked systematically the validity of this approach comparing the results with the complete no-click evolution [34]. Fixing  $p_{\text{site}} = 1$ , parametrizing the measurement rate as  $p_{\text{meas}} = \gamma dt$  and expanding at first order in  $dt$  we get

$$|\psi(t + dt)\rangle = \hat{M} e^{-i\hat{H}dt} |\psi(t)\rangle \simeq e^{-i\hat{\mathcal{H}}_{\text{eff}}dt} |\psi(t)\rangle, \quad (7)$$

where we have introduced the non-hermitian Hamiltonian

$$\hat{\mathcal{H}}_{\text{eff}} = \hat{\mathcal{H}} - i\hat{\Gamma} = J^x \sum_{i=1}^{L-1} \hat{\sigma}_i^x \hat{\sigma}_{i+1}^x - i\frac{\gamma}{2} \sum_{i=1}^L \frac{\hat{\sigma}_i^z + \mathbb{I}}{2}. \quad (8)$$

Remarkably, the continuous monitoring generates a purely imaginary transverse field, proportional to the strength of the measurement  $\gamma$ , which does not commute with the Hamiltonian  $\hat{\mathcal{H}}$  generating the unitary dynamics, in our case an Ising exchange term along  $x$ . The no-click dynamics is therefore described by a non-hermitian TFIM, whose physics is completely controlled by the parameter  $g = \gamma/J^x$ , i.e. the ratio between the strength of the two non-commuting part of the non-hermitian Hamiltonian. Thus, also in the no-click dynamics we do expect that the amount of correlation in the system can increase as  $g$  is increased, due to the competition

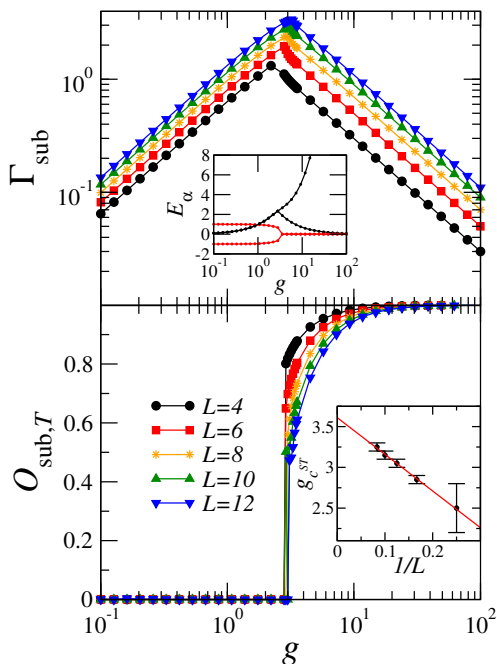


Figure 4. Subradiant Transition in the Non-Hermitian Hamiltonian. Top panel: Subradiant width  $\Gamma_{\text{sub}}$  as a function of  $g$ . (Inset: Real and Imaginary part of the subradiant states as a function of  $g$ ). Bottom panel: overlap  $O_{\text{sub},T}$  between the subradiant state and the Zeno state  $|T\rangle$ , for  $L = 6, 8, 10, 12$ . (Inset: finite size scaling of the critical point  $g_c^{ST}$ ). Here we set  $dt = 10^{-2}$ ,  $J^x = 1$ .

between  $\hat{\mathcal{H}}$  and  $\hat{\Gamma}$ . We notice that non-Hermitian extensions of classical Ising models have a long tradition in statistical physics [35, 36], while the non-Hermitian TFIM has been much less explored. Since this model is not PT symmetric [37], its many-body spectrum is in general complex. The non-Hermitian evolution at long times drive the state to the eigenstate of  $\hat{\mathcal{H}}_{\text{eff}}$  with smaller imaginary part since  $|\psi(t)\rangle = \sum_{\alpha=1}^N \langle \tilde{\alpha} | \psi(0) \rangle e^{-itE_{\alpha}} |\alpha\rangle$  where  $\langle \tilde{\alpha} |$  ( $|\alpha\rangle$ ) are the left/right eigenvectors of  $\hat{\mathcal{H}}_{\text{eff}}$ ,  $E_{\alpha} = \omega_{\alpha} - i\Gamma_{\alpha}$  are the corresponding complex eigenvalues and  $N$  is the dimension of the Hilbert space. Remarkably,  $\hat{\mathcal{H}}_{\text{eff}}$  undergoes a so called subradiance transition [26–33] at  $g = g_c^{ST}$ , which is signaled by a non-analytic behavior of the eigenvalue with smaller imaginary part,  $\Gamma_{\text{sub}} = \min(\Gamma_{\alpha})$ , as we see in Figure 4 (top panel). The real part of the subradiant eigenvalue vanishes for  $g = g_c^{ST}$ , where it merges with an anti-subradiant partner, and remains pinned there for  $g > g_c^{ST}$  (top panel, inset). The transition to the subradiant regime is sharp also at finite size and the critical value of  $g$  slowly shifts with size. A finite size scaling analysis of the critical point  $g_c^{ST}$  (bottom panel, inset) gives  $g_c^{ST} = \mathcal{A} + \mathcal{B} L^{-1}$  with  $\mathcal{A} = 3.61 \pm 0.02$  and  $\mathcal{B} = 4.5 \pm 0.1$ . We can thus infer the behavior in the thermodynamic limit ( $\lim_{L \rightarrow \infty} g_c^{ST} = \mathcal{A}$ ). Further insights on the subradiance transition can be obtained by looking at the effective non-Hermitian Hamil-

tonian in the large  $g$  regime, where we can estimate the structure of  $\Gamma_{\text{sub}}$  analytically. We get

$$\lim_{g \rightarrow \infty} |\text{sub}\rangle = |T\rangle, \quad \lim_{g \rightarrow \infty} \Gamma_{\text{sub}} = 0. \quad (9)$$

The overlap  $O_{\text{sub},T}$  shows a sharp non-analyticity as a function of  $g$  (see Fig. 4, bottom panel) which seems to become more and more continuous as the size of the system is increased. Remarkably its behavior matches with  $O_{\psi,T}$ , the order parameter defined for the full stochastic evolution (see Fig.1).

**Analytical results** – The non-hermitian TFIM in Eq. (8) can be diagonalised exactly using the Jordan-Wigner representation of the spin operators into fermionic creation/annihilation operators and a generalised Bogoliubov transformation, as we discuss more in detail in Ref. [34]. The final result, in terms of new fermionic operators  $\hat{\gamma}_k^{\dagger}/\hat{\gamma}_k$  reads (fixing  $J^x = 1$ )

$$\hat{\mathcal{H}}_{\text{eff}} = \sum_{k>0} \Lambda_k \left( \hat{\gamma}_k^{\dagger} \hat{\gamma}_k + \hat{\gamma}_{-k}^{\dagger} \hat{\gamma}_{-k} - 1 \right) - i \frac{g}{g_c} L, \quad (10)$$

where the quasiparticle spectrum reads [34]

$$\Lambda_k = 2\sqrt{1 - (g/g_c)^2 + ig/g_c \cos k} \equiv \Delta_k + i\Sigma_k, \quad (11)$$

and we have introduced the critical coupling  $g_c = 4$ . The behavior of this spectrum is particularly interesting around  $k = \pi/2$ : for  $g < g_c$  the real-part is gapped, with a gap closing (in the thermodynamic limit  $L \rightarrow \infty$ ) as  $\Delta = \Delta_{k=\pi/2} \sim \sqrt{1 - (g/g_c)^2}$  (with  $\Sigma_{k=\pi/2} = 0$ ); for  $g > g_c$  the real-part of the energy spectrum remains pinned to zero ( $\Delta_{k=\pi/2} = 0$ ) while a gap opens up in the imaginary part,  $\Sigma = \Sigma_{k=\pi/2} \sim \sqrt{(g/g_c)^2 - 1}$ . Right at the critical point,  $g = g_c$ , the spectrum around  $k = \pi/2$  acquires a very unusual power-law scaling [34]

$$\Lambda_k \sim |\pi/2 - k|^{1/2} [1 + i \text{sign}(k - \pi/2)]. \quad (12)$$

As we show in Ref. [34] this has direct consequences in the structure of the two subradiant states merging at  $g_c$ , whose structure factor is strongly peaked at  $k \simeq \pi/2$  before the transition. Finally, from the quasiparticle spectrum (11) we can obtain the many-body eigenstates [34], in particular the emerging subradiant state which has an (intensive) complex energy [34]

$$\varepsilon_{\text{sub}} = \frac{1}{2\pi} \int_{-\pi}^0 \Lambda_k dk - i \frac{g}{g_c}. \quad (13)$$

At weak coupling,  $g/g_c \ll 1$ , the subradiant eigenvalue has a real-part which does not depend on  $g$  and a linearly growing imaginary part,  $\varepsilon_{\text{sub}} \sim 1 - ig/g_c$ . At strong coupling instead,  $g/g_c \gg 1$  we find from Eq. (13) a purely imaginary eigenvalue, which goes to zero as  $\varepsilon_{\text{sub}} \sim -2ig_c/g$ , in agreement with our exact numerical calculations (see Fig. 4) and with Eq.(9).

**Conclusions** – In this work we have shown that the many-body QZE in a quantum Ising chain, where strong continuous monitoring of the transverse magnetization leads to a complete freezing of the system, appears sharply upon increasing the ratio between measurement strength and coherent (entangling) interaction. Crucially, this transition is not encoded in the average dynamics, but it is rather controlled by rare fluctuations which we show are perfectly captured by looking at the no-click evolution. In the limit of continuous measurements this reduces to a non-hermitian TFIM which we show, using exact numerics and a mapping to fermions, to undergo a sharp subradiance transition characterized by a non-analytic behavior of the slowest decay mode and by a gap closing in the quasiparticle spectrum. This work establish a rather general important connection between many body QZE, subradiance transition in non-hermitian systems and rare fluctuation of the stochastic dynamics of a measured quantum many-body system. Future directions include the investigation of the role of spatially inhomogeneous measurements ( $p_{\text{site}} < 1$ ) leading to dilute disorder [38–41], different initial conditions and higher dimensionality.

**Acknowledgments** – The computations were performed on the Collège de France IPH computer cluster. We acknowledge support from the ANR grant “NonEquMat” (ANR-19-CE47-0001).

---

\* alberto.biella@college-de-france.fr

† marco.schiro@college-de-france.fr; On Leave from: Institut de Physique Théorique, Université Paris Saclay, CNRS, CEA, F-91191 Gif-sur-Yvette, France

- [1] H. M. Wiseman and G. J. Milburn, *Quantum Measurement and Control* (Cambridge University Press, 2009).
- [2] B. Misra and E. C. G. Sudarshan, *Journal of Mathematical Physics* **18**, 756 (1977), <https://doi.org/10.1063/1.523304>.
- [3] A. Peres, *American Journal of Physics* **48**, 931 (1980), <https://doi.org/10.1119/1.12204>.
- [4] W. M. Itano, D. J. Heinzen, J. J. Bollinger, and D. J. Wineland, *Phys. Rev. A* **41**, 2295 (1990).
- [5] P. Facchi, H. Nakazato, and S. Pascazio, *Phys. Rev. Lett.* **86**, 2699 (2001).
- [6] P. Facchi and S. Pascazio, *Phys. Rev. Lett.* **89**, 080401 (2002).
- [7] A. Signoles, A. Facon, D. Grosso, I. Dotsenko, S. Haroche, J.-M. Raimond, M. Brune, and S. Gleyzes, *Nature Physics* **10**, 715 (2014).
- [8] K. Snizhko, P. Kumar, and A. Romito, *Phys. Rev. Research* **2**, 033512 (2020).
- [9] L. M. Duan, M. D. Lukin, J. I. Cirac, and P. Zoller, *Nature* **414**, 413 (2001).
- [10] A. S. Sørensen and K. Mølmer, *Phys. Rev. Lett.* **91**, 097905 (2003).
- [11] C. W. Chou, H. de Riedmatten, D. Felinto, S. V. Polyakov, S. J. van Enk, and H. J. Kimble, *Nature* **438**, 828 (2005).
- [12] N. Roch, M. E. Schwartz, F. Motzoi, C. Macklin, R. Vijay, A. W. Eddins, A. N. Korotkov, K. B. Whaley, M. Sarovar, and I. Siddiqi, *Phys. Rev. Lett.* **112**, 170501 (2014).
- [13] J. Kong, R. Jiménez-Martínez, C. Troullinou, V. G. Lucivero, G. Tóth, and M. W. Mitchell, *Nature Communications* **11**, 2415 (2020).
- [14] N. Syassen, D. M. Bauer, M. Lettner, T. Volz, D. Dietze, J. J. García-Ripoll, J. I. Cirac, G. Rempe, and S. Dürr, *Science* **320**, 1329 (2008), <https://science.sciencemag.org/content/320/5881/1329.full.pdf>.
- [15] Y. S. Patil, S. Chakram, and M. Vengalattore, *Phys. Rev. Lett.* **115**, 140402 (2015).
- [16] H. Fröml, A. Chiocchetta, C. Kollath, and S. Diehl, *Phys. Rev. Lett.* **122**, 040402 (2019).
- [17] Y. Li, X. Chen, and M. P. A. Fisher, *Phys. Rev. B* **98**, 205136 (2018).
- [18] B. Skinner, J. Ruhman, and A. Nahum, *Phys. Rev. X* **9**, 031009 (2019).
- [19] M. Szyniszewski, A. Romito, and H. Schomerus, *Phys. Rev. B* **100**, 064204 (2019).
- [20] S. Choi, Y. Bao, X.-L. Qi, and E. Altman, *Phys. Rev. Lett.* **125**, 030505 (2020).
- [21] C.-M. Jian, Y.-Z. You, R. Vasseur, and A. W. W. Ludwig, *Phys. Rev. B* **101**, 104302 (2020).
- [22] X. Turkeshi, R. Fazio, and M. Dalmonte, *Phys. Rev. B* **102**, 014315 (2020).
- [23] D. Bernard, T. Jin, and O. Shpielberg, *EPL (Europhysics Letters)* **121**, 60006 (2018).
- [24] X. Cao, A. Tilloy, and A. D. Luca, *SciPost Phys.* **7**, 24 (2019).
- [25] Y. Fuji and Y. Ashida, *Phys. Rev. B* **102**, 054302 (2020).
- [26] Y. Ashida, Z. Gong, and M. Ueda, “Non-hermitian physics,” (2020), arXiv:2006.01837 [cond-mat.mes-hall].
- [27] R. H. Dicke, *Phys. Rev.* **93**, 99 (1954).
- [28] M. Gross and S. Haroche, *Physics Reports* **93**, 301 (1982).
- [29] G. L. Celardo and L. Kaplan, *Phys. Rev. B* **79**, 155108 (2009).
- [30] N. Auerbach and V. Zelevinsky, *Reports on Progress in Physics* **74**, 106301 (2011).
- [31] A. Biella, F. Borgonovi, R. Kaiser, and G. L. Celardo, *EPL (Europhysics Letters)* **103**, 57009 (2013).
- [32] W. Guerin, M. O. Araújo, and R. Kaiser, *Phys. Rev. Lett.* **116**, 083601 (2016).
- [33] I. Rotter and J. P. Bird, *Reports on Progress in Physics* **78**, 114001 (2015).
- [34] See Supplemental Material.
- [35] M. E. Fisher, *Phys. Rev. Lett.* **40**, 1610 (1978).
- [36] J. L. Cardy, *Phys. Rev. Lett.* **54**, 1354 (1985).
- [37] C. M. Bender, *Journal of Physics: Conference Series* **631**, 012002 (2015).
- [38] A. B. Harris, *Journal of Physics C: Solid State Physics* **7**, 3082 (1974).
- [39] R. B. Stinchcombe, *Journal of Physics C: Solid State Physics* **14**, L263 (1981).
- [40] F. Thompson and R. R. P. Singh, *Phys. Rev. E* **99**, 032129 (2019).
- [41] T. Senthil and S. Sachdev, *Phys. Rev. Lett.* **77**, 5292 (1996).

**SUPPLEMENTAL MATERIAL FOR:  
MANY-BODY QUANTUM ZENO EFFECT AND MEASUREMENT-INDUCED SUBRADIANCE  
TRANSITION**

**I. EXCESS ENTANGLEMENT**

As discussed in the main text, we quantify the *excess entanglement* via the quantity  $\Theta_E$  defined in Eq.(6). In this appendix we show how  $\Theta_E$  depends on  $p_{\text{site}}$ . In Fig.S1 we show  $\Theta_E$  for several different values of  $p_{\text{site}}$ . Curves collapse when plotted against  $g p_{\text{site}}$  [with  $g$  defined in Eq.(4)]. This result shows that that for this specific quantity

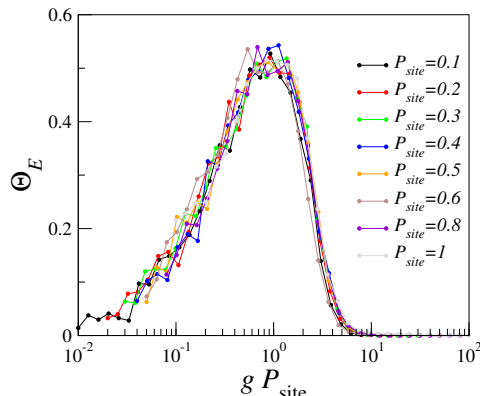


Figure S1. Measurement-induced entanglement  $\Theta_E$  as a function of  $g p_{\text{site}}$  for several values of  $p_{\text{site}}$ . Here we set  $N_{\text{real}} = 100$ ,  $dt = 10^{-2}$ ,  $L = 8$ ,  $J^x = 1$ .

the control parameter is given by

$$g p_{\text{site}} = \frac{p_{\text{tot}}}{J^x dt}, \quad (\text{S1})$$

where  $p_{\text{tot}} = p_{\text{site}} p_{\text{meas}}$ , indicating that the spatial density and the strength of the measurements play an equivalent role in the generation of the excess entanglement.

**II. ONSET OF THE ZENO EFFECT**

In this section we show appearance of the Zeno dynamics as  $g$  is increased. The onset of the SZ phase can be inspected monitoring the probability distribution of the local magnetization  $P(m^z)$  which represents the probability of having a certain value of the local magnetization during the dynamics  $m^z = \langle \psi(t) | \hat{\sigma}_i^z | \psi(t) \rangle, \forall i$ . For  $g \lesssim 1$  the distribution  $P(m^z)$  explores almost uniformly all the possible values of the magnetization with two peaks progressively emerging at  $m_-^z$  and  $m_+^z$ , located respectively at  $m_z < 0$  and  $m_z \simeq 1$ . For  $g \gtrsim 1$  the structure of the probability distribution change dramatically. Beside the *usual* peak at  $m^z \approx 1$ , the second peak at  $m_-^z$  sharper and moves toward  $m^z = -1$  as  $g$  is increased. Finally, for  $g \gg 1$  the distribution is a delta function peaked at  $m^z = -1$ . In the top left panel we also show the behaviour of  $m_-^z$  as a function of  $g$ .

We stress that the value of  $m^z$  unambiguously determine the quantum state since the local single-site density matrix can be parametrized as  $\hat{\rho}_{\text{loc}} = \frac{1}{2} (\mathbb{I} + m^z \hat{\sigma}^z)$ . It is clear that the only free parameter is  $m^z$ , therefore the structure of  $P(m^z)$  directly gives information about the onset of the Zeno effect (i.e. the system state is mostly frozen next to one of the measurement eigenstates, yet rarely performs quantum jumps between them). In Fig.S2 we show the probability distribution of the local magnetization  $P(m^z)$  which represents the probability of having a certain value of the local magnetization during the dynamics  $m^z = \langle \psi(t) | \hat{\sigma}_i^z | \psi(t) \rangle, \forall i$ .

In the top left panel we compare the position of the peak at  $m_-^z$  with the magnetization of the subradiant state  $\langle \text{sub} | \hat{\Sigma}^z | \text{sub} \rangle / L$ . The two curves show a perfect agreement for  $g > 4$ .

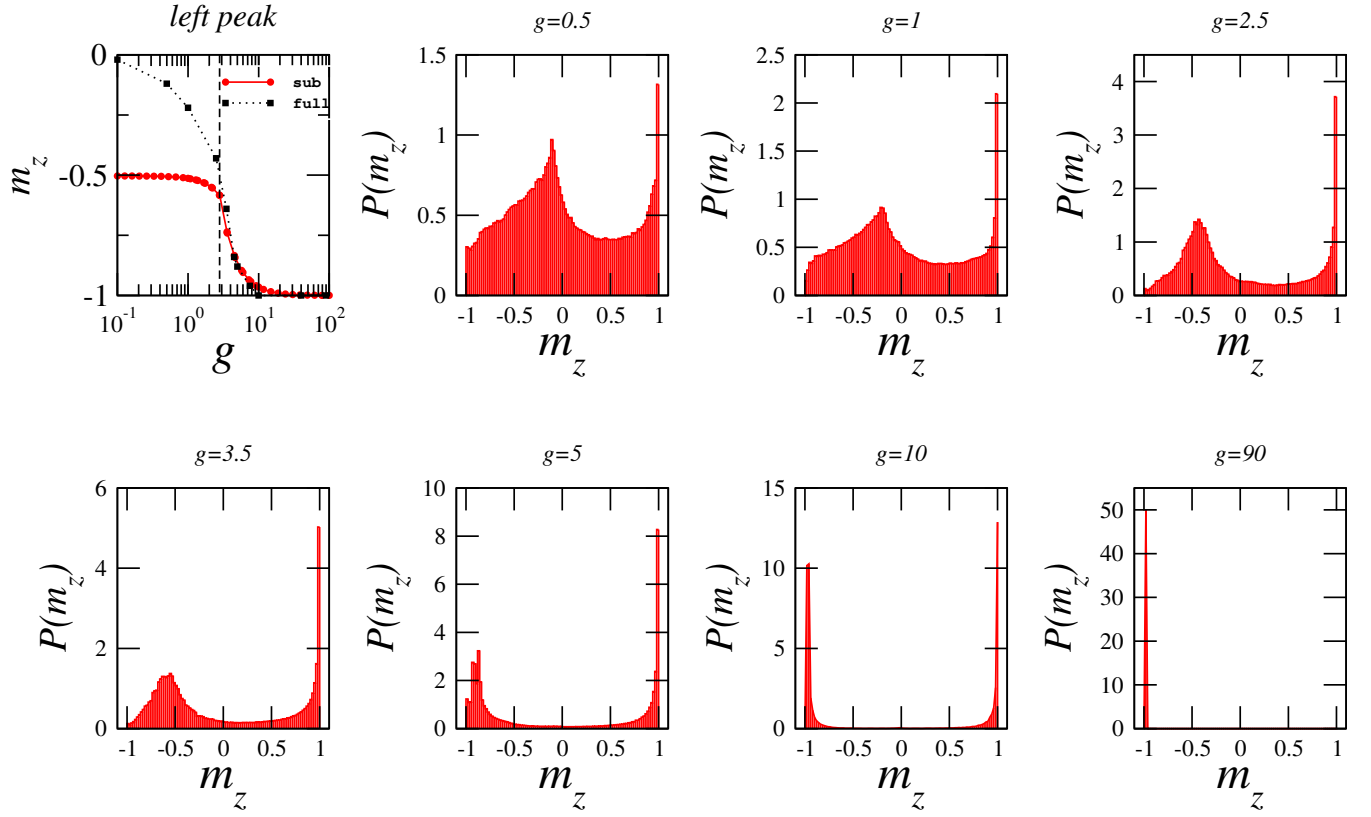


Figure S2. Probability distribution of the local magnetization  $P(m_z)$  for different values of  $g$ . In the top left panel we show the position of  $m_z^-$ , the leftmost peak of  $P(m_z)$ . We also compare it with magnetization of the subradiant state of  $\hat{\mathcal{H}}_{\text{eff}}$ . Here we set  $p_{\text{site}} = 1$ ,  $dt = 10^{-2}$ ,  $L = 8$ ,  $J^x = 1$ ,  $N_{\text{real}} = 100$ .

### III. VALIDITY OF THE NON-HERMITIAN EFFECTIVE HAMILTONIAN

In this appendix we test the validity of the non-Hermitian effective Hamiltonian  $\hat{\mathcal{H}}_{\text{eff}}$ . To this purpose we compare the *full* no-click evolution with the one generated by the  $\hat{\mathcal{H}}_{\text{eff}}$  [Eq.(7)] for different values of  $g$ .

As we can see from Fig.S3 we dynamics induced by  $\hat{\mathcal{H}}_{\text{eff}}$  reproduce exactly the no-click evolution of the entanglement entropy  $S_E$  for  $g \lesssim 1$ . After this threshold the results for the entanglement entropy slightly differ quantitatively but behaves qualitatively in the same way.

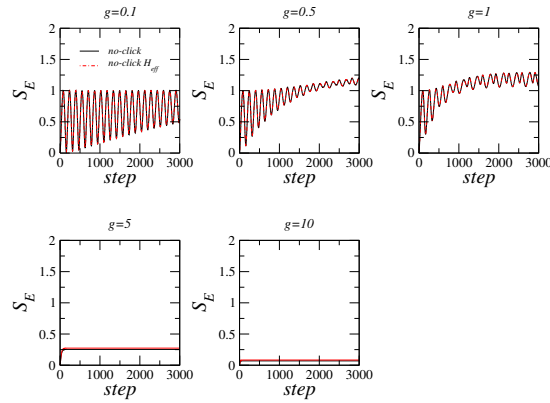


Figure S3. Comparison between the *full* no-click evolution with the one generated by the  $\hat{\mathcal{H}}_{\text{eff}}$  [Eq.(7)] for different values of  $g$ . Here we set  $dt = 10^{-2}$ ,  $L = 8$ ,  $J^x = 1$ .

#### IV. DIAGONALIZATION OF NON-HERMITIAN QUANTUM ISING MODEL

We consider the non-Hermitian Transverse Field Ising Model (TFIM) introduced in the main text, whose Hamiltonian reads

$$\hat{\mathcal{H}}_{\text{eff}} = \hat{\mathcal{H}} - i\hat{\Gamma} = J^x \sum_{i=1}^{L-1} \hat{\sigma}_i^x \hat{\sigma}_{i+1}^x - i\frac{\gamma}{2} \sum_{i=1}^L \frac{\hat{\sigma}_i^z + 1}{2} \quad (\text{S2})$$

and we take periodic boundary conditions for the spin  $\sigma_{L+1}^x = \sigma_1^x$ . Using the Jordan-Wigner transformation, which maps spin-1/2 operators to fermions through the identities

$$\sigma_j^x = \hat{K}_j (\hat{c}_j + \hat{c}_j^\dagger), \quad (\text{S3})$$

$$\sigma_j^z = 1 - 2\hat{c}_j^\dagger \hat{c}_j, \quad (\text{S4})$$

where the so called *string* operator  $\hat{K}_j$ , defined as

$$\hat{K}_j = \left[ \prod_{l<j} (1 - 2\hat{c}_l^\dagger \hat{c}_l) \right], \quad (\text{S5})$$

ensures the proper fermionic algebra. We can rewrite Eq. (S2) as

$$\begin{aligned} \hat{\mathcal{H}}_{\text{eff}} = & J^x \sum_{i=1}^{L-1} \left( \hat{c}_i^\dagger \hat{c}_{i+1} + \hat{c}_i \hat{c}_{i+1}^\dagger + \text{H.c.} \right) - i\frac{\gamma}{2} \sum_{i=1}^L \left( 1 - \hat{c}_i^\dagger \hat{c}_i \right) + \\ & + (-1)^{N_F} J^x \left( \hat{c}_L^\dagger \hat{c}_1 + \hat{c}_L \hat{c}_1^\dagger + \text{H.c.} \right) \end{aligned} \quad (\text{S6})$$

In the last expression  $N_F = \sum_{i=1}^L \hat{c}_i^\dagger \hat{c}_i$  is the total number of fermions and  $(-1)^{N_F}$  the associated parity. We notice that in the Hamiltonian case (purely real transverse field) the fermionic parity is conserved and as such the last term is just a phase that can be handled by proper choice of boundary conditions, i.e. by posing  $\hat{c}_{L+1} = (-1)^{N_F+1} \hat{c}_1$ . In the non-Hermitian case this is in general not the case, however one can show that starting from an initial state which is eigenstate of the fermionic parity (as it is our case here) the latter will remain conserved throughout the evolution. Therefore we fixed the parity to be even (as we start from the  $N_F = 0$  sector), which corresponds to anti-periodic boundary conditions (ABC). Going to Fourier space, and fixing the values of  $k$  appropriate for ABC, we obtain

$$\hat{\mathcal{H}}_{\text{eff}} = \sum_k \varepsilon_k \hat{c}_k^\dagger \hat{c}_k + J \sum_k i \sin k \left( \hat{c}_k^\dagger \hat{c}_{-k}^\dagger - \hat{c}_{-k} \hat{c}_k \right) - i\frac{\gamma}{2} L \quad (\text{S7})$$

with  $\varepsilon_k = i\gamma/2 + 2J \cos k$ . We notice that last term on the right hand side, deriving from Eq. (S6) which is crucial to ensure the non-Hermitian Hamiltonian has a positive definite imaginary part. Restricting the sum to positive values of  $k$  and introducing Nambu-Gorkov spinor notation  $\Psi_k = \left( \hat{c}_k, \hat{c}_{-k}^\dagger \right)^\text{T}$  we get  $\hat{\mathcal{H}}_{\text{eff}} = \sum_{k>0} \bar{\Psi}_k h_k \Psi_k - i\frac{\gamma}{4} L$  where we defined the generalized Bogoliubov matrix

$$h_k = \begin{pmatrix} \varepsilon_k & -i\eta_k \\ i\eta_k & -\varepsilon_k \end{pmatrix}, \quad (\text{S8})$$

where  $\eta_k = -2J^x \sin k$ . We can then diagonalise the matrix  $h_k$  and introduce new fermionic operators  $\gamma_k$  to obtain

$$\hat{\mathcal{H}}_{\text{eff}} = \sum_{k>0} \Lambda_k \left( \hat{\gamma}_k^\dagger \hat{\gamma}_k + \hat{\gamma}_{-k}^\dagger \hat{\gamma}_{-k} - 1 \right) - i\frac{\gamma}{4} L, \quad (\text{S9})$$

where the quasiparticle spectrum reads

$$\Lambda_k = 2J^x \sqrt{1 - (g/g_c)^2 + ig/g_c \cos k} \equiv \Delta_k + i\Sigma_k \quad (\text{S10})$$

and we have introduced the critical coupling  $g_c = 4$ . As stated in the main text, the behavior of this spectrum is particularly interesting around  $k = \pi/2$ : for  $g < g_c$  the real-part is gapped, with a gap closing (in the thermodynamic

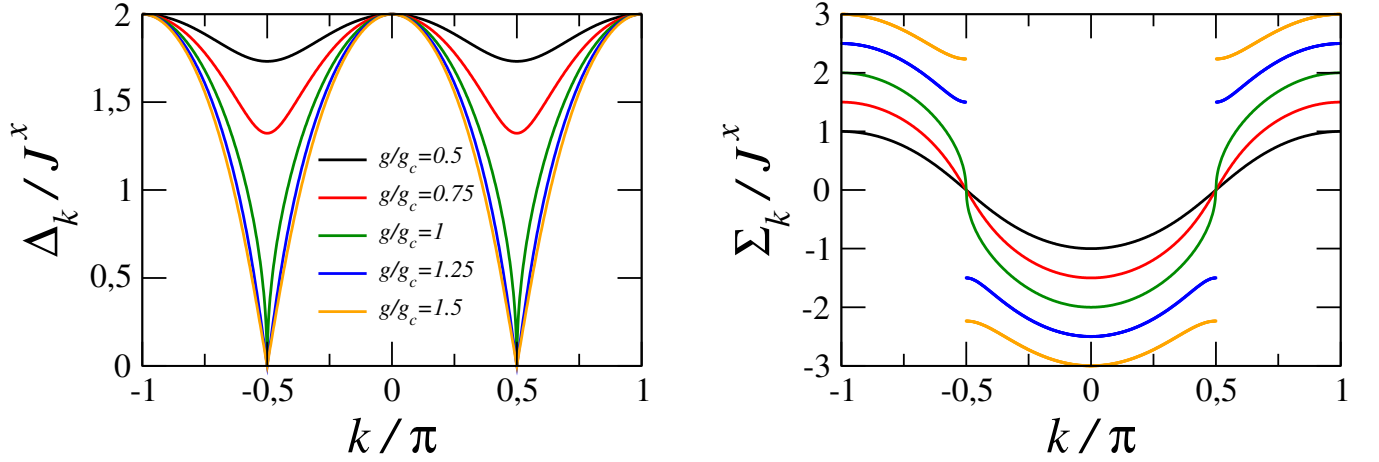


Figure S4. Quasiparticle spectrum  $\Lambda_k$  of the non-Hermitian TFIM, Eq (S10), for different values of  $g = \gamma/J^x$ . The real part (left panel),  $\text{Re}\Lambda_k = \Delta_k$ , displays two minima at  $k = \pm\pi/2$  which touch zero as  $g$  approaches the critical value  $g_c$  and remain pinned there for  $g > g_c$ . At the critical point,  $g = g_c$ , the real-part of the quasiparticle spectrum goes near  $k \sim \pi/2$  as  $\Delta_k \sim |\pi/2 - k|^{1/2}$ . The imaginary part (right panel),  $\text{Im}\Lambda_k = \Sigma_k$ , is continuous and gapless for  $g < g_c$ , while a gap opens at  $\pi/2$  for  $g > g_c$ . At the critical point,  $g = g_c$ , the imaginary-part of the quasiparticle spectrum goes near  $k \sim \pi/2$  as  $\Sigma_k \sim \text{sign}(k - \pi/2)|\pi/2 - k|^{1/2}$ .

limit  $L \rightarrow \infty$ ) as  $\Delta = \Delta_{k=\pi/2} \sim \sqrt{1 - (g/g_c)^2}$  (with  $\Sigma_{k=\pi/2} = 0$ ); for  $g > g_c$  the real-part of the energy spectrum remains pinned to zero ( $\Delta_{k=\pi/2} = 0$ ) while a gap opens up at  $k = \pi/2$  in the imaginary part,  $\Sigma = \Sigma_{k=\pi/2} \sim \sqrt{(g/g_c)^2 - 1}$ . Right at the critical value,  $g = g_c$ , both real and imaginary part of the quasiparticle energy display a very unusual power-law scaling for  $k$  around  $k = \pi/2$ , i.e.  $\Delta_k \sim |\pi/2 - k|^{1/2}$  and  $\Sigma_k \sim \text{sign}(k - \pi/2)|\pi/2 - k|^{1/2}$ . The real and imaginary part of the quasiparticle spectrum is shown in Fig.S4 for different values of  $g/g_c$  across the transition. Once the Hamiltonian is diagonalised we can write down any eigenstate in terms of the occupation numbers of the fermions  $\hat{\gamma}_k, \hat{\gamma}_k^\dagger$ . Specifically the vacuum state reads

$$|\text{vac}\rangle = \prod_{k>0} \hat{\gamma}_{-k} \hat{\gamma}_k |0\rangle \quad (\text{S11})$$

with intensive energy  $\varepsilon_{\text{vac}} = E_{\text{vac}}/L = -\frac{1}{L} \sum_{k>0} \Lambda_k - i\frac{\gamma}{4}$  which reads (in the thermodynamic limit)

$$\varepsilon_{\text{vac}}/2J^x = -\int_0^\pi \frac{dk}{2\pi} \sqrt{1 - (g/g_c)^2 + ig/g_c \cos k} - i\frac{g}{2g_c}. \quad (\text{S12})$$

Similarly, any excited state of the form

$$|\{n_k\}\rangle = \prod_k (\hat{\gamma}_k^\dagger)^{n_k} |\text{vac}\rangle \quad (\text{S13})$$

with  $n_k = 0, 1$  such that  $\sum_k n_k = N_F$ , given the even parity sector, has eigenvalue

$$E(\{n_k\}) = E_{\text{vac}} + \sum_k n_k \Lambda_k. \quad (\text{S14})$$

For example, the state  $|T\rangle = \bigotimes_{i=1}^L |-\rangle_i$  (that is the exact subradiant state of  $\hat{\mathcal{H}}_{\text{eff}}$  in the  $g/g_c \rightarrow \infty$  limit) can be written in this fermionic language as the maximally occupied state, with  $n_k = 1$  for all  $k$ . It has eigenvalue

$$\varepsilon_{\text{sub}}/2J^x = \int_{-\pi}^0 \frac{dk}{2\pi} \sqrt{1 - (g/g_c)^2 + ig/g_c \cos k} - i\frac{g}{2g_c}. \quad (\text{S15})$$

At weak coupling,  $g/g_c \ll 1$ , we can expand the square root and obtain for the subradiant eigenvalue  $\varepsilon_{\text{sub}}/2J^x \sim 1/2 - ig/2g_c$ , namely a real-part which does not depend on  $g$  and a linearly growing imaginary part. At strong coupling instead,  $g/g_c \gg 1$  we find a purely imaginary subradiant eigenvalue, which goes to zero as  $\varepsilon_{\text{sub}}/2J^x \sim -ig_c/g$ , such that as expected we get  $\lim_{g/g_c \rightarrow \infty} \varepsilon_{\text{sub}} = 0$ , in agreement with the exact numerical calculations shown in Figure 4 of the main text (see inset).

### V. $k$ -MODE OCCUPANCY

Here we show the  $k$ -mode occupancy of the subradiant and anti-subradiant state (the many-body state that becomes degenerate with the subradiant at the transition) defined as

$$\begin{aligned} \langle \hat{n}_k \rangle &= \langle \hat{\sigma}_k^+ \hat{\sigma}_k^- \rangle \\ &= \frac{2}{L+1} \sum_{i,j=1}^L \sin(ki) \sin(kj) \langle \hat{\sigma}_i^+ \hat{\sigma}_j^- \rangle, \end{aligned} \quad (\text{S16})$$

with  $k = n\pi/(L+1)$ ,  $n = 1, \dots, L$  as imposed by open boundary conditions and where we used the Fourier transform of the spin operators

$$\hat{\sigma}_k^+ = \sqrt{\frac{2}{L+1}} \sum_{i=1}^L \sin(ki) \hat{\sigma}_i^+. \quad (\text{S17})$$

The result is shown in Fig.S5. The anti-subradiant state (bottom panel) remains mainly populates the  $k = \pi/2$  mode

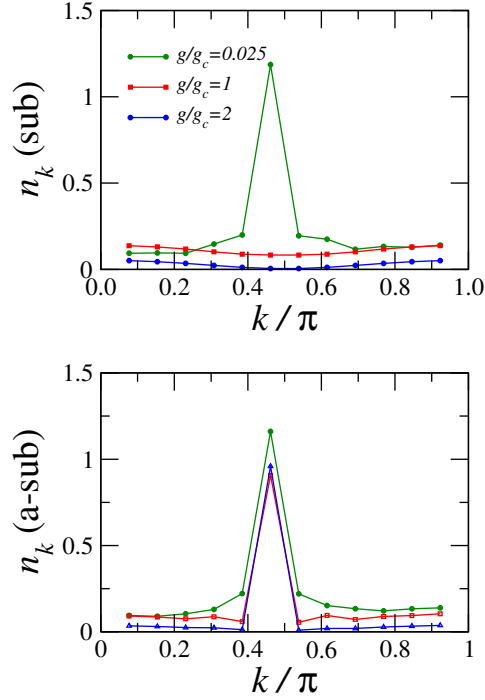


Figure S5. Population in  $k$ -space [see Eq.(S16)] of the subradiant (top panel) and anti-subradiant (bottom panel) state. Here we set  $J^x = 1$  and vary  $\gamma$  in order to change the dimensionless coupling  $g$ .

of the chain as  $g$  is varied across the transition. The superradiant state (top panel) is peaked around  $k = \pi/2$  for  $g/g_c < 1$ . After the transition the  $k$ -mode distribution is sharply depleted since  $|\text{sub}\rangle \rightarrow |T\rangle$  as  $g/g_c \rightarrow \infty$ .